Nonlinear Bending Analysis of FG Porous Beams Reinforced with Graphene Platelets Under Various Boundary Conditions by Ritz Method

Dang Xuan Hung, Huong Quy Truong(✉), and Tran Minh Tu

National University of Civil Engineering, 55 Giai Phong Road, Hai Ba Trung District, Hanoi, Vietnam
{hungdx,truonghq,tutm}@nuce.edu.vn

Abstract. This paper deals with the nonlinear bending response of functionally graded porous beams reinforced by graphene platelets (GPLs) with various boundary conditions using the Ritz method. Based on the trigonometric shear deformation beam theory and the von Kárman type of geometrical nonlinearity strains, the system of nonlinear governing equations is derived using the minimum total potential energy principle. This system of nonlinear equations is then solved by the Newton–Raphson method. The comparison with the available published results validates the obtained results. The effects of the porosity distribution patterns, the porosity coefficient, the GPL reinforcements, the slenderness ratios and the boundary conditions on the nonlinear deflection of the FGP porous beam are also investigated.

Keywords: Porous beam · Nonlinear bending · Ritz method · Trigonometric shear deformation beam theory · Graphene platelet reinforcement

1 Introduction

Functionally graded materials (FGMs) are a class of composites that are firstly invented by Japanese scientists in 1984. FGMs are characterized by a continuous variation in both composition and material properties in one or more directions, thus eliminating interface problems and diminishing the stress concentration that normally exists in conventional laminated composites [1, 2].

Porous materials (metal foams) are a new class of FGMs characterized by low density, lightweight, good stiffness and excellent energy absorption, Porosities inside metal foams can be distributed in different manners. Their mechanical properties are significantly influenced by the amount of porosities and their pattern of distribution. To archive desire material properties, graded non-uniform porosities are introduced to produce FG metal foams which have been proved to have better structural response than the normal uniform foams and are investigated by the increasing number of researchers [3–10].

Introducing nanofillers into porous materials is a practical way to strengthen their mechanical properties and maintain their potential for lightweight structures simultaneously. The properties of such materials can be significantly improved with the addition of

N. Tien Khiem et al. (Eds.): *Modern Mechanics and Applications*, LNME, pp. 72–86, 2022.
https://doi.org/10.1007/978-981-16-3239-6_6

nanofillers in the form of carbon nanotubes (CNTs) and graphene platelets (GPLs). Thus, carbon nanotube reinforced beams and plates have been extensively studied to examine their static and dynamic response [11–15]. Until now, static and dynamic analysis of GPL reinforced structures is still at the beginning stage [16–20].

A nonlinear static analysis is required for any static application in which the stiffness of the entire structure changes during the loading scenario. Many works focused on nonlinear behaviours of beams and plates are reported in the existing literature. Feng et al. [21] studies the nonlinear bending behavior of Timoshenko multi-layer polymer nanocomposite beams reinforced with GPLs using Ritz method. Shen et al. [22] studied the large amplitude vibration of functionally graded graphene-reinforced composite laminated plates resting on an elastic foundation and in thermal environments based on a higher-order shear deformation plate theory and perturbation technique. Wu et al. [12] analyzed nonlinear vibration of imperfect FG-CNTRC beams is based on the first-order shear deformation beam theory and von Kármán geometric nonlinearity. Ke et al. [15] investigated the nonlinear free vibration of FG nanocomposite beams reinforced by single-walled carbon nanotubes (SWCNTs) based on Timoshenko beam theory. Barati et al. [20] used a refined beam model to investigate the post-buckling behavior of geometrically imperfect porous beams reinforced with graphene platelets. Yas and Rahimi [23] presented thermal buckling of FG porous nanocomposite beams subjected to a thermal gradient using the generalized differential quadrature method.

This paper deals with the geometrically nonlinear bending analysis of functionally graded porous beams reinforced by graphene platelets with various boundary conditions using the Ritz method. GPLs are distributed in the thickness direction with uniform and nonuniform patterns. Uniform, symmetric, and asymmetric distributions of porosity have been considered. After conducting the validate example, the effects of the porosity distribution patterns, the porosity coefficient, the GPL reinforcements, the slenderness ratios and the boundary conditions on the nonlinear deflection of the FGP porous beam are investigated in detail.

2 Material Properties

Consider a beam with thickness h, width b, and length L defined in the Cartesian coordinate system (x, z) as shown in Fig. 1. The porosity distributes within the thickness according to the symmetric, asymmetric and uniform laws below [24].

$$\begin{cases} \psi(z) = \cos(\pi z/h) \\ \psi(z) = \cos\left(\pi z/2h + \frac{\pi}{4}\right) \\ \psi(z) = \psi_0 \end{cases} \tag{1}$$

This porosity distribution leads to a variety of material properties as follows.

$$\begin{cases} E_z = E_c[1 - e_0\psi(z)] \\ G_z = E_z/[2(1 + \nu_z)] \\ \rho_z = \rho_c[1 - e_m\psi(z)] \end{cases} \tag{2}$$

Where E_c and ρ_c denote the Young modulus and the mass density of the material without porosity, respectively; E_1', E_2' $(\rho_1,\ \rho_2)$ denote the maximum, minimum Young's

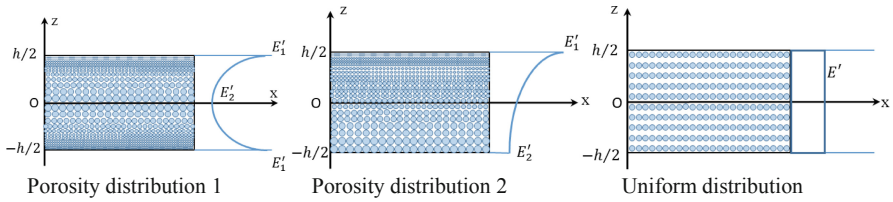

Fig. 1. Porosity distribution: symmetric, asymmetric and uniform laws

modulus (mass density) without GPLs of the non-uniform porosity distribution and that of the uniform law is denoted by $E^{'}$; The porosity coefficient e_0 and the mass density coefficient e_m are defined by $e_0 = 1 - E_2'/E_1'$ and $e_m = 1 - \rho_2/\rho_1$.

Based on the relationship between the mechanical properties of closed-cell cellular solids (3) that is fitted from statistical Gaussian Random Fields model [25],

$$\frac{E_z}{E_c} = \left[\left(\frac{\rho_z}{\rho_c} + 0.121\right)/1.121\right]^{2.3} \qquad \left(0.15 < \frac{\rho_z}{\rho_c} < 1\right) \tag{3}$$

the coefficient of mass density e_m is determined and presented by.

$$e_m = \frac{1.121\left[1 - \sqrt[2.3]{1 - e_0\psi(z)}\right]}{\psi(z)} \tag{4}$$

The coefficient ψ_0 will be determined assuming all the uniform and non-uniform porosity beams have the same mass, that leads to:

$$\psi_0 = \frac{1}{e_0} - \frac{1}{e_0}\left[\left(\frac{1}{h\rho_c}\int_{-h/2}^{h/2}\rho_z dz + 0.121\right)/1.121\right]^{2.3} \tag{5}$$

Poisson's ratio ν_z can be obtained as [26]

$$\nu_z = 0.221p' + \nu_c\left(0.342p'^2 - 1.21p' + 1\right) \tag{6}$$

where ν_c denotes the Poisson's ratio of pure matrix materials without pores and

$$p' = 1 - \frac{\rho_z}{\rho_1} = 1.121\left(1 - \sqrt[2.3]{1 - e_0\psi(z)}\right) \tag{7}$$

The GPLs disperse within the beam with the volume fraction V_{GPL} varies functionally graded along the z axis. Three different GPL dispersion patterns (8), denoted by A, B and C, are considered for each porosity distribution and graphically presented in Fig. 2.

$$\begin{cases} V_{GPL} = s_{i1}[1 - \cos(\pi z/h)] & \text{Pattern A} \\ V_{GPL} = s_{i2}[1 - \cos(\pi z/2h + \pi/4)] & \text{Pattern B} \\ V_{GPL} = s_{i3} & \text{Pattern C} \end{cases} \tag{8}$$

Where the maximum value $\left(s_{ij} - i, j = 1, 2, 3\right)$ of the GPL volume fraction depends on the porosity distribution and need to be determined via the relation between the weight fraction W_{GPL} of GPL nanofillers and its volume content.

$$\frac{W_{GPL}}{W_{GPL}.\rho_m + \rho_{GPL} - W_{GPL}.\rho_{GPL}} \int_{-h/2}^{h/2} \frac{\rho_z}{\rho_c} dz = \int_{-h/2}^{h/2} V_{GPL} \frac{\rho_z}{\rho_c} dz \tag{9}$$

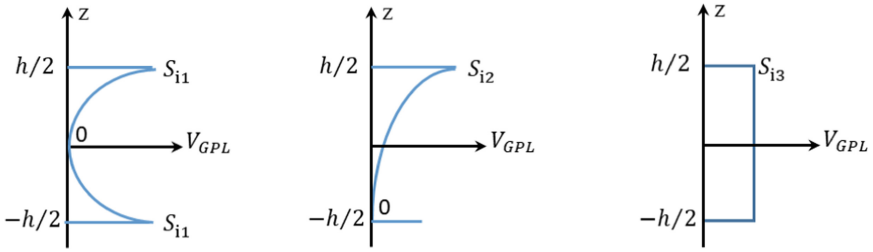

GPL dispersion A GPL dispersion B GPL dispersion C

Fig. 2. GPL dispersion patterns

The effective Young's modulus E_c is determined by the Halpin-Tsai micromechanics model [27–29] as

$$E_c = \frac{3}{8}\left(\frac{1 + \xi_L^{GPL}.\eta_L^{GPL}.V_{GPL}}{1 - \eta_L^{GPL}.V_{GPL}}\right)E_m + \frac{5}{8}\left(\frac{1 + \xi_W^{GPL}.\eta_W^{GPL}.V_{GPL}}{1 - \eta_W^{GPL}.V_{GPL}}\right)E_m \tag{10}$$

in which $\xi_L^{GPL} = 2L_{GPL}/t_{GPL}$, $\xi_W^{GPL} = 2w_{GPL}/t_{GPL}$ and E_m is Young's modulus of the metal matrix; L_{GPL}, t_{GPL} and w_{GPL} are the GPL's average length, thickness and width; η_L^{GPL}, η_W^{GPL} can be computed by

$$\begin{aligned} \eta_L^{GPL} &= \frac{E_{GPL} - E_m}{E_{GPL} + \xi_L^{GPL} E_m} \\ \eta_W^{GPL} &= \frac{E_{GPL} - E_m}{E_{GPL} + \xi_W^{GPL} E_m} \end{aligned} \tag{11}$$

The mass density and Poisson's ratio of the nanocomposite are given by the rule of the mixture as

$$\begin{aligned} \rho_c &= \rho_{GPL} \cdot V_{GPL} + \rho_m V_m \\ \nu_c &= \nu_{GPL} \cdot V_{GPL} + \nu_m V_m \end{aligned} \tag{12}$$

in which ρ_{GPL}, ν_{GPL} and V_{GPL} (ρ_m , ν_m and $V_m = 1 - V_{GPL}$) are mass density, Poisson's ratio, and volume fraction of GPLs (metals), respectively.

3 Formulations

The displacement field of the beam is assumed having the trigonometric model [30]

$$\begin{aligned} u(x,z,t) &= u_0(x,t) - zw_{0,x} + \tfrac{h}{\pi}\sin\left(\tfrac{\pi z}{h}\right)\theta_x \\ w(x,z,t) &= w_0(x,t); \end{aligned} \tag{13}$$

where u_0; w_0 are the axial and transverse displacement components on the mid-plane ($z = 0$) of the beam; θ_x is the mid-plan rotation of transverse normal.

The strains field from the kinematic equations incorporating nonlinear strain components by von Karman's assumptions are stated as follows

$$\begin{cases} \varepsilon_{xx} = u_{0,x} - zw_{0,xx} + \tfrac{h}{\pi}\sin\left(\tfrac{\pi z}{h}\right)\theta_{x,x} + \tfrac{1}{2}w_{0,x}^2 \\ \gamma_{xz} = \cos\left(\tfrac{\pi z}{h}\right)\theta_x \end{cases} \tag{14}$$

The stress components in the beam are determined from Hooke's law.

$$\begin{Bmatrix} \sigma_{xx} \\ \sigma_{xz} \end{Bmatrix} = \begin{pmatrix} C_{11} & 0 \\ 0 & C_{66} \end{pmatrix} \begin{Bmatrix} \varepsilon_{xx} \\ \gamma_{xz} \end{Bmatrix} \tag{15}$$

where

$$C_{11} = \frac{E_z}{1-\nu_z^2} \qquad C_{66} = G_z = \frac{E_z}{2(1+\nu_z)} \tag{16}$$

with ν_z is the Poisson's ratio.

The elastic potential energy of the beam is determined by.

$$U = \frac{1}{2}\int_A \int_0^L (\sigma_{xx}\varepsilon_{xx} + \sigma_{xz}\gamma_{xz})dxdA \tag{17}$$

Introducing (14) into (17) one obtains.

$$\begin{aligned} U = \frac{1}{2}\int_A \int_0^L (\sigma_{xx}\varepsilon_{xx} + \sigma_{xz}\gamma_{xz})dxdA = \frac{1}{2}\int_0^L \begin{pmatrix} Au_{0,x}^2 + Dw_{0,x}^2 + H^*\theta_{x,x}^2 + 0.25Aw_{0,x}^4 \\ +2Bu_{0,x}w_{0,xx} + 2B^*u_{0,x}\theta_{x,x} + Au_{0,x}w_{0,x}^2 \\ +2D^*w_{0,xx}\theta_{x,x} + Bw_{0,xx}w_{0,x}^2 + B^*\theta_{x,x}w_{0,x}^2 \end{pmatrix} dx \\ + \frac{1}{2}\int_0^L \left(A^*\theta_x^2\right)dx \end{aligned} \tag{18}$$

where the stiffness components are

$$\begin{aligned} &\left(A;\, B;\, D;\, B^*;\, D^*;\, H^*\right) = bE_z \int_{-h/2}^{h/2} \left[1;\, -z;\, z^2;\, \tfrac{h}{\pi}\sin\left(\tfrac{\pi z}{h}\right);\, \tfrac{hz}{\pi}\sin\left(\tfrac{\pi z}{h}\right);\, \tfrac{h^2}{\pi^2}\sin^2\left(\tfrac{\pi z}{h}\right)\right]dz \\ &A^* = b\int_{-h/2}^{h/2} G_z \cos^2\left(\tfrac{\pi z}{h}\right)dz; \end{aligned} \tag{19}$$

The potential energy of external loads V is written as.

$$V = -b\int_0^L q_0 w_0 dx \tag{20}$$

where q_0 is the transverse distributed load applied at the top surface of the beam ($z = h/2$). The total potential energy is defined by.

$$\Pi = U + V \tag{21}$$

4 Ritz Method

The Ritz method is based on the expansion of the displacement components in series of algebraic functions that satisfy the boundary conditions [31].

$$u_0(x,t) = \sum_{i=1}^{n} c_i \varphi_i; \quad w_0(x,t) = \sum_{j=1}^{n} d_j \psi_j; \quad \theta_x = \sum_{k=1}^{n} e_k \phi_k \tag{22}$$

c_i, d_j, e_k are the unknown coefficients need to be determined and φ_i, ψ_j, ϕ_k are the admissible functions that have the form of increased order polynomials.

$$\varphi_i = f_u x^{i-1}; \quad \psi_j = f_w x^{j-1}; \quad \phi_k = f_\theta x^{k-1} \quad (i,j,k = 1,2,\ldots,n) \tag{23}$$

where n is the number of terms in the expansion and $f_* = x^{p_*}(L-x)^{q_*}$ with p_*, q_* are the boundary condition representative coefficients as in Table 1 and $(* = u, w, \theta)$.

Table 1. Value of the boundary condition representative coefficients (Clamped-C; Hinged-H; Free-F)

BCs	C-C	H-H	C-F	C-H
p_u	1	1	1	1
q_u	1	1	0	0
p_w	2	1	2	2
q_w	2	1	0	1
p_θ	1	0	1	1
q_θ	1	0	0	0

Nonlinear governing equations of the bending beam are obtained using the principle of minimum total potential energy. The stationary condition of the total potential energy yields.

$$\frac{\partial \Pi}{\partial c_i} = 0; \quad \frac{\partial \Pi}{\partial d_j} = 0; \quad \frac{\partial \Pi}{\partial e_k} = 0 \quad (i,j,k = 1,\ldots,n) \tag{24}$$

As the system of Eqs. (24) is nonlinear, it should be solved by an iterative algorithm, such as the Newton-Raphson method that is used in this research.

5 Numerical Results and Discussions

In this section, we firstly test the convergence and the validation of the numerical results. Then, the effect of GPL dispersion patterns, weight fractions (wt.%), porosity coefficients, boundary conditions and slenderness ratios on the nonlinear bending behavior of the functionally graded porous nanocomposite beam are also carried out. The material properties and geometrical parameters of the GPLs and the copper metal matrix are referred to [26] and are listed below:

$w_{GPL} = 1.5\,\mu m$; $L_{GPL} = 2.5\,\mu m$; $t_{GPL} = 1.5\,\eta m$; $E_{GPL} = 1.01\,TPa$; $\rho_{GPL} = 1602.5\,kg/m^3$; $\nu_{GPL} = 0.186$; $E_m = 130\,GPa$; $\rho_m = 8960\,kg/m^3$; $\nu_m = 0.34$.

In all analyses, dimensionless deflections and uniformly distributed loads are defined as:

$$\overline{w} = \frac{w}{h}; \qquad \overline{q}_0 = \frac{12 \cdot q_0 \cdot L^3}{Eh^3} \tag{25}$$

a. *Convergence test*

This test aims at studying the convergence of the bending deflection when the number of terms of the series expansion (n) increases. Table 2 shows the dimensionless deflection of the beam with porosity distribution 1, GPLs dispersion pattern A, various boundary conditions H-H, C-C, C-H, C-F, and under dimensionless load $\overline{q}_0 = 100$. It is obviously observed that the results converge when the number of terms of the series expansion from $n = 9$. Hence, this number will be used in all analyses below.

Table 2. Convergence of the maximum dimensionless deflection when the number of terms in the expansion increases ($L/h = 20$; $e_0 = 0.5$; $W_{GPL} = 1\%$)

N	$H-H$	$C-C$	$C-H$	$C-F$
2	1.7949617	1.3902453	1.5942035	8.13876650
4	1.8733061	1.4928277	1.6819245	9.98223780
6	1.8697857	1.5236849	1.7032373	10.2700112
7	1.8708479	1.5232990	1.7048970	10.3028099
8	1.8709485	1.5222694	1.7034279	10.3188111
9	1.8709256	1.5225556	1.7044578	10.3274922
10	1.8709243	1.5270215	1.7066475	10.3322133
11	1.8709295	1.5269125	1.7068624	10.3350252

b. *Validation*

The validation of the present results is performed by comparing with those of Zhang [32]. In [32], the author studied the nonlinear bending of an aluminum beam with H-H,

C-C boundary conditions, under a transverse uniform load by using the third-order shear deformation theory and Ritz method. The material properties are $E = 70$ MPa, $\nu = 0.3$; length-to-thick ratio $L/h = 20$.

The maximum dimensionless deflections $\overline{w}_{\max}$ are presented in Table 3. An excellent agreement is found and this confirms the reliability of the present approach.

Table 3. Comparison of maximum dimensionless deflection of the isotropic beam under various boundary conditions (BCs.)

BCs	Beam theories	Dimensionless uniformly distributed load $q_0.L^4/E/h^4$					
		1	8	30	80	120	200
H-H	PSDBT [32]	0.1474	0.5980	1.053	1.515	1.748	2.086
	Present	0.1474	0.5979	1.053	1.515	1.748	2.087
C-C	PSDBT [32]	0.0321	0.2460	0.7042	1.221	1.475	1.837
	Present	0.0321	0.2450	0.6972	1.221	1.468	1.835

iii. *Effect of porous and GPL distribution laws*

The porous beams reinforced by graphene platelets with $L/h = 20$ are subjected to uniformly distributed load ($\overline{q}_0 = 100$) and various boundary conditions. The GPL weight fraction and the porosity coefficient are $W_{PGL} = 1\%$ and $e_0 = 0.5$. The combined effect of porosity distribution laws and GPL dispersion patterns on maximum dimensionless deflection are presented in Table 4.

Table 4. Maximum dimensionless deflection with various boundary conditions and different combinations of porosity distribution law and GPLs dispersion pattern

L/h	BCs	Porosity distribution type	$\overline{q}_0 = 100$		
			GPL dispersion pattern		
			A (sym.)	B (asym.)	C (uniform)
20	H-H	1 (sym.)	1.87084	1.81011	1.90367
		2 (asym.)	1.81897	1.77270	1.85013
		3 (uniform)	1.91155	1.84638	1.92413
	C-C	1 (sym.)	1.52329	1.60475	1.59554
		2 (asym.)	1.58860	1.64765	1.64506
		3 (uniform)	1.59802	1.66172	1.65444

(*continued*)

Table 4. (*continued*)

L/h	BCs	Porosity distribution type	$\bar{q}_0 = 100$		
			GPL dispersion pattern		
			A (sym.)	B (asym.)	C (uniform)
	C-H	1 (sym.)	1.70489	1.70541	1.75250
		2 (asym.)	1.70431	1.70643	1.74336
		3 (uniform)	1.75834	1.74970	1.78728
	C-F	1 (sym.)	10.30280	10.52577	10.46521
		2 (asym.)	10.46160	10.47703	10.52795
		3 (uniform)	10.65099	10.75091	10.68225

Results indicate that in general, the combination of the GPL distribution patterns and the porosity distribution laws produces different deflection values. Under different boundary conditions, each porosity distribution law has specific GPL distribution pattern to achieve maximum stiffness of beams. In most cases (C-C, C-F; CH boundary conditions), the beams with symmetric GPL and porosity distribution possess high flexural stiffness due to the high GPL concentration and less porosity near the top and bottom surface. Hence, detailed investigation (unless otherwise specified) is performed by assuming the symmetrical distribution for porosity and GPL in the beam.

iv. *Effect of porosity coefficient*

Consider a porous beam reinforced by graphene platelets with $L/h = 20$, $W_{PGL} = 1\%$, subjected to various levels of uniformly distributed load $\bar{q}_0 = 0;\ 25;\ 50;\ 75;\ 100;\ 125;\ 150;\ 175;\ 200$. The maximum dimensionless deflections of the beam for different values of porosity coefficients $e_0 = 0;\ 0.2;\ 0.4;\ 0.6;\ 0.8$ are tabulated in Table 5.

Table 5. Maximum dimensionless deflection under various level load and different values of porosity coefficient.

BCs	e_0	$\bar{q}_0$								
		0	25	50	75	100	125	150	175	200
H-H	0.0	0	0.9665	1.2764	1.4878	1.6538	1.7928	1.9136	2.0212	2.1187
	0.2	0	1.0139	1.3360	1.5559	1.7287	1.8734	1.9992	2.1113	2.2128
	0.4	0	1.0703	1.4073	1.6375	1.8184	1.9700	2.1019	2.2193	2.3257
	0.6	0	1.1400	1.4955	1.7386	1.9298	2.0901	2.2294	2.3536	2.4661
	0.8	0	1.2315	1.6116	1.8718	2.0766	2.2483	2.3976	2.5307	2.6514

(*continued*)

Table 5. (*continued*)

BCs	e_0	$\overline{q}_0$								
		0	25	50	75	100	125	150	175	200
C-C	0.0	0	0.5467	0.8876	1.1258	1.3113	1.4650	1.5974	1.7143	1.8195
	0.2	0	0.5870	0.9439	1.1917	1.3845	1.5442	1.6818	1.8032	1.9125
	0.4	0	0.6355	1.0111	1.2705	1.4720	1.6390	1.7828	1.9098	2.0240
	0.6	0	0.6963	1.0949	1.3687	1.5812	1.7572	1.9087	2.0426	2.1630
	0.8	0	0.7793	1.2080	1.5006	1.7276	1.9154	2.0772	2.2200	2.3485
C-H	0.0	0	0.7735	1.1007	1.3212	1.4927	1.6353	1.7586	1.8679	1.9665
	0.2	0	0.8186	1.1586	1.3877	1.5660	1.7143	1.8425	1.9562	2.0588
	0.4	0	0.8722	1.2276	1.4672	1.6537	1.8088	1.9430	2.0620	2.1694
	0.6	0	0.9385	1.3131	1.5658	1.7626	1.9263	2.0679	2.1935	2.3077
	0.8	0	1.0264	1.4265	1.6965	1.9068	2.0819	2.2334	2.3685	2.4930
C-F	0.0	0	5.1097	6.7102	7.8252	8.7093	9.4534	10.1021	10.6808	11.2055
	0.2	0	5.4501	7.1531	8.3394	9.2798	10.0712	10.7609	11.3761	11.9339
	0.4	0	5.8423	7.6627	8.9305	9.9352	10.7804	11.5169	12.1737	12.7691
	0.6	0	6.3040	8.2615	9.6242	10.7035	11.6112	12.4019	13.1068	13.7458
	0.8	0	6.8715	8.9950	10.4718	11.6405	12.6228	13.4781	14.2405	14.9314

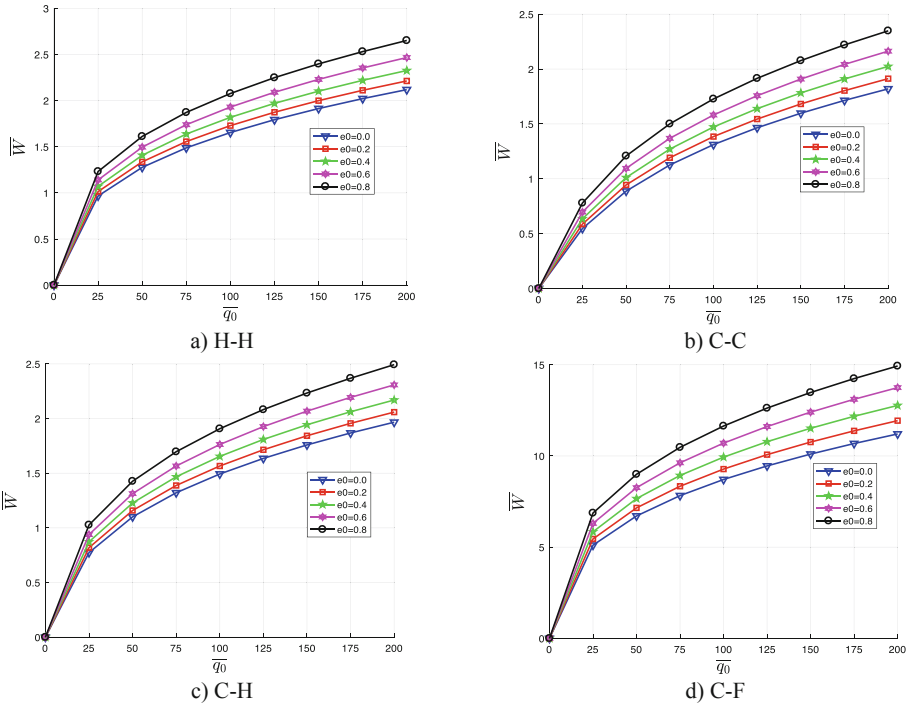

Fig. 3. Effect of porosity coefficients on the maximum dimensionless deflection of the reinforced porous beam

The load-deflection curves for different values of porosity coefficients are presented in Fig. 3. It can be observed that the maximum deflections increase nonlinearly as the uniformly distributed loads increase for all values of porosity coefficients. The maximum deflections are bigger as the porosity coefficients increase, this is because the stiffness of the beams decreases as the porosity coefficients increase.

e. Effect of GPL weight fraction
The same beam with abovementioned input geometric and loading data is considered. Maximum dimensionless deflection of the porous beam with porosity coefficient $e_0 = 0.4$ and different values of GPL weight fraction $W_{PGL} = 0\%;\ 0.2\%;\ 0.4\%;\ 0.6\%;\ 0.8\%$ are tabulated in Table 6. Effects of GPL weight fraction on maximum dimensionless deflection are illustrated by loads-deflection curves in Fig. 4. Results show that as GPL volume fraction is increased, the stiffness of the beams is significantly improved. This causes the deflection to decrease for all boundary conditions of the beams.

Table 6. Maximum dimensionless deflection under various load levels and different values of GPL weight fraction.

BCs	W_{PGL}	$\bar{q}_0$								
		0	25	50	75	100	125	150	175	200
H-H	0.0	0	1.2375	1.6049	1.8577	2.0571	2.2246	2.3705	2.5006	2.6185
	0.2	0	1.1864	1.5444	1.7903	1.9840	2.1467	2.2882	2.4144	2.5289
	0.4	0	1.1425	1.4925	1.7324	1.9213	2.0797	2.2176	2.3405	2.4518
	0.6	0	1.1041	1.4472	1.6819	1.8666	2.0214	2.1561	2.2761	2.3848
	0.8	0	1.0703	1.4073	1.6375	1.8184	1.9701	2.1019	2.2193	2.3257
C-C	0.0	0	0.8489	1.2617	1.5407	1.7572	1.9369	2.0918	2.2290	2.3525
	0.2	0	0.7812	1.1842	1.4576	1.6697	1.8456	1.9972	2.1312	2.2520
	0.4	0	0.7246	1.1181	1.3865	1.5947	1.7673	1.9159	2.0473	2.1656
	0.6	0	0.6767	1.0611	1.3247	1.5295	1.6991	1.8451	1.9742	2.0904
	0.8	0	0.6355	1.0111	1.2705	1.4720	1.6390	1.7828	1.9098	2.0240
C-H	0.0	0	1.0623	1.4445	1.7035	1.9060	2.0750	2.2246	2.3583	2.4793
	0.2	0	1.0038	1.3781	1.6312	1.8288	1.9936	2.1363	2.2662	2.3838
	0.4	0	0.9538	1.3210	1.5691	1.7625	1.9236	2.0631	2.1872	2.3020
	0.6	0	0.9104	1.2714	1.5149	1.7047	1.8626	1.9993	2.1205	2.2308
	0.8	0	0.8722	1.2276	1.4672	1.6537	1.8088	1.9430	2.0620	2.1694
C-F	0.0	0	6.6034	8.5794	9.9566	11.0477	11.9656	12.7653	13.4786	14.1253
	0.2	0	6.3624	8.2882	9.6302	10.6936	11.5882	12.3676	13.0627	13.6929
	0.4	0	6.1611	8.0454	9.3583	10.3988	11.2740	12.0367	12.7168	13.3333
	0.6	0	5.9899	7.8396	9.1281	10.1492	11.0083	11.7568	12.4243	13.0294
	0.8	0	5.8423	7.6627	8.9305	9.9352	10.7805	11.5169	12.1737	12.7692

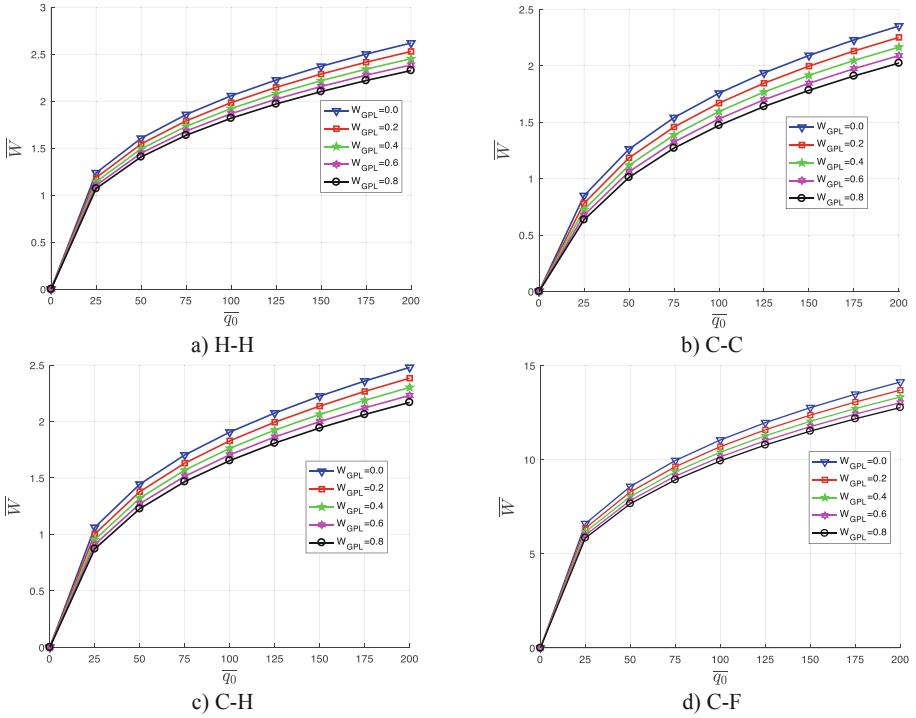

a) H-H b) C-C

c) C-H d) C-F

Fig. 4. Effect of GPL weight fraction on maximum dimensionless deflection

f. *Effect of the slenderness ratio*

In this example, we consider a beam with input parameters: $e_0 = 0.4$, $W_{PGL} = 1\%$, subjected to uniformly distributed load $\overline{q}_0 = 100$. Maximum dimensionless deflections of the porous beam with various values of slenderness ratio $L/h = 5\,;\ 10\,;\ 20\,;\ 30\,;\ 40\,;\ 50$ are shown in Table 7.

Table 7. Effect of slenderness ratio on the maximum dimensionless deflection.

BCs	L/h					
	5	10	20	30	40	50
H-H	1.0855	1.4091	1.8184	2.1019	2.3258	2.5139
C-C	0.8609	1.0830	1.4720	1.7645	1.9981	2.1942
C-H	0.9734	1.2561	1.6537	1.9359	2.1593	2.3468
C-F	6.1399	7.7835	9.9352	11.4748	12.7085	13.7525

The effect of slenderness ratio on the maximum dimensionless deflection is depicted in Fig. 5. It is clearly observed that the beam's deflection augments nonlinearly when

the slenderness ratio increases. This effect is the strongest for the cantilever beam (C-F) and is demonstrated by the separate line of the C-F beam in Fig. 5.

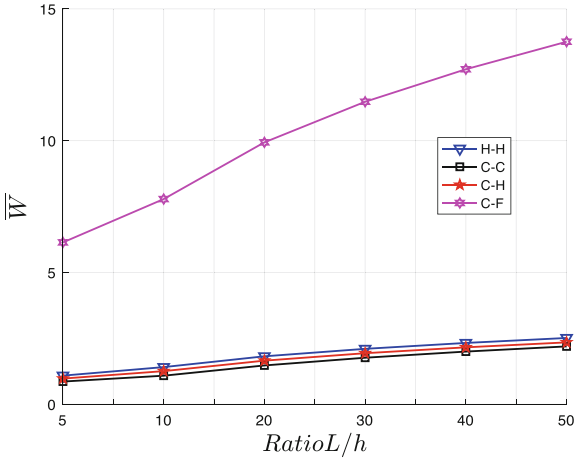

Fig. 5. Effect of slenderness ratio on the maximum dimensionless deflection

6 Conclusions

In this paper, the Ritz method is used to study the geometrically nonlinear bending behavior of the metal foam beams reinforced by GPLs under various boundary conditions. The validation examples are conducted and showed a good agreement with existing results in a published article. Numerical results reveal that the porosity distribution law, porosity coefficient, GPL distribution pattern, GPL weight fraction, and slenderness ration of the beam and boundary conditions have great influences on the nonlinear bending response of the beam. In addition, the effect of the porosity coefficient on the beam deflection is more significant than that of the GPL weight fraction.

Acknowledgements. This research is funded by the Vietnam National Foundation for Science and Technology Development (NAFOSTED) (Grant No. 107.02-2018.322). The financial support is gratefully acknowledged.

References

1. Koizumi, M.: FGM activities in Japan. Compos. B Eng. **28**(1–2), 1–4 (1997)
2. Gupta, A., Talha, M.: Recent development in modeling and analysis of functionally graded materials and structures. Prog. Aerosp. Sci. **79**, 1–14 (2015)
3. Magnucki, K., Malinowski, M., Kasprzak, J.: Bending and buckling of a rectangular porous plate. Steel Compos. Struct. **6**(4), 319–333 (2006)

4. Chen, D., Yang, J., Kitipornchai, S.: Elastic buckling and static bending of shear deformable functionally graded porous beam. Compos. Struct. **133**, 54–61 (2015)
5. Wattanasakulpong, N., Chaikittiratana, A., Pornpeerakeat, S.: Chebyshev collocation approach for vibration analysis of functionally graded porous beams based on third-order shear deformation theory. Acta. Mech. Sin. **34**(6), 1124–1135 (2018). https://doi.org/10.1007/s10409-018-0770-3
6. Phuong, N.T.B., et al.: Bending analysis of functionally graded beam with porosities resting on elastic foundation based on neutral surface position. J. Sci. Technol. Civ. Eng. (STCE)-NUCE **13**(1), 33–45 (2019)
7. Zhao, J., et al.: Free vibrations of functionally graded porous rectangular plate with uniform elastic boundary conditions. Compos. B Eng. **168**, 106–120 (2019)
8. Tu, T.M., et al.: Nonlinear buckling and post-buckling analysis of imperfect porous plates under mechanical loads. J. Sandwich Struct. Mater. **22**(6), 1910–1930 (2020)
9. Thang, P.T., et al.: Elastic buckling and free vibration analyses of porous-cellular plates with uniform and non-uniform porosity distributions. Aerosp. Sci. Technol. **79**, 278–287 (2018)
10. Akbaş, ŞD.: Vibration and static analysis of functionally graded porous plates. J. Appl. Comput. Mech. **3**(3), 199–207 (2017)
11. Wattanasakulpong, N., Ungbhakorn, V.: Analytical solutions for bending, buckling and vibration responses of carbon nanotube-reinforced composite beams resting on elastic foundation. Comput. Mater. Sci. **71**, 201–208 (2013)
12. Wu, H., Yang, J., Kitipornchai, S.: Nonlinear vibration of functionally graded carbon nanotube-reinforced composite beams with geometric imperfections. Compos. B Eng. **90**, 86–96 (2016)
13. Shen, H.-S.: Nonlinear bending of functionally graded carbon nanotube-reinforced composite plates in thermal environments. Compos. Struct. **91**(1), 9–19 (2009)
14. Zhu, P., Lei, Z., Liew, K.M.: Static and free vibration analyses of carbon nanotube-reinforced composite plates using finite element method with first order shear deformation plate theory. Compos. Struct. **94**(4), 1450–1460 (2012)
15. Ke, L.-L., Yang, J., Kitipornchai, S.: Nonlinear free vibration of functionally graded carbon nanotube-reinforced composite beams. Compos. Struct. **92**(3), 676–683 (2010)
16. Song, M., Kitipornchai, S., Yang, J.: Free and forced vibrations of functionally graded polymer composite plates reinforced with graphene nanoplatelets. Compos. Struct. **159**, 579–588 (2017)
17. Yang, J., Wu, H., Kitipornchai, S.: Buckling and postbuckling of functionally graded multilayer graphene platelet-reinforced composite beams. Compos. Struct. **161**, 111–118 (2017)
18. Feng, C., Kitipornchai, S., Yang, J.: Nonlinear free vibration of functionally graded polymer composite beams reinforced with graphene nanoplatelets (GPLs). Eng. Struct. **140**, 110–119 (2017)
19. Shen, H.-S., Xiang, Y., Lin, F.: Nonlinear bending of functionally graded graphene-reinforced composite laminated plates resting on elastic foundations in thermal environments. Compos. Struct. **170**, 80–90 (2017)
20. Barati, M.R., Zenkour, A.M.: Post-buckling analysis of refined shear deformable graphene platelet reinforced beams with porosities and geometrical imperfection. Compos. Struct. **181**, 194–202 (2017)
21. Feng, C., Kitipornchai, S., Yang, J.: Nonlinear bending of polymer nanocomposite beams reinforced with non-uniformly distributed graphene platelets (GPLs). Compos. B Eng. **110**, 132–140 (2017)
22. Shen, H.-S., Xiang, Y., Lin, F.: Nonlinear vibration of functionally graded graphene-reinforced composite laminated plates in thermal environments. Comput. Methods Appl. Mech. Eng. **319**, 175–193 (2017)

23. Yas, M.-H., Rahimi, S.: Thermal buckling analysis of porous functionally graded nanocomposite beams reinforced by graphene platelets using Generalized differential quadrature method. Aerospace Science and Technology, 106261 (2020)
24. Chen, D., Yang, J., Kitipornchai, S.: Nonlinear vibration and postbuckling of functionally graded graphene reinforced porous nanocomposite beams. Compos. Sci. Technol. **142**, 235–245 (2017)
25. Roberts, A.P., Garboczi, E.J.: Elastic moduli of model random three-dimensional closed-cell cellular solids. Acta Mater. **49**(2), 189–197 (2001)
26. Kitipornchai, S., Chen, D., Yang, J.: Free vibration and elastic buckling of functionally graded porous beams reinforced by graphene platelets. Mater. Des. **116**, 656–665 (2017)
27. Rafiee, M.A., et al.: Enhanced mechanical properties of nanocomposites at low graphene content. ACS Nano **3**(12), 3884–3890 (2009)
28. Tjong, S.C.: Recent progress in the development and properties of novel metal matrix nanocomposites reinforced with carbon nanotubes and graphene nanosheets. Mater. Sci. Eng. R Rep. **74**(10), 281–350 (2013)
29. Yeh, M.-K., Tai, N.-H., Liu, J.-H.: Mechanical behavior of phenolic-based composites reinforced with multi-walled carbon nanotubes. Carbon **44**(1), 1–9 (2006)
30. Touratier, M.: An efficient standard plate theory. Int. J. Eng. Sci. **29**(8), 901–916 (1991)
31. Pradhan, K., Chakraverty, S.: Free vibration of Euler and Timoshenko functionally graded beams by Rayleigh-Ritz method. Compos. B Eng. **51**, 175–184 (2013)
32. Zhang, D.-G.: Nonlinear bending analysis of FGM beams based on physical neutral surface and high order shear deformation theory. Compos. Struct. **100**, 121–126 (2013)